

# Phenylboronic acid modification augments the lysosome escape and antitumor efficacy of a cylindrical polymer brush-based prodrug

**Ruonan Wang**

Nanjing University

**Changfeng Yin**

Nanjing University

**Changren Liu**

Nanjing University

**Ying Sun**

Nanjing University

**Panpan Xiao**

Nanjing University

**Jia Li**

Nanjing University

**Shuo Yang**

Nanjing University

**Wei Wu** (✉ [wuwei@nju.edu.cn](mailto:wuwei@nju.edu.cn))

Nanjing University

**Xiqun Jiang**

Nanjing University <https://orcid.org/0000-0003-0483-0282>

---

## Article

**Keywords:** Phenylboronic acid, cylindrical polymer brushes, nanomedicines

**Posted Date:** September 8th, 2021

**DOI:** <https://doi.org/10.21203/rs.3.rs-877913/v1>

**License:**   This work is licensed under a Creative Commons Attribution 4.0 International License.

[Read Full License](#)

---

**Version of Record:** A version of this preprint was published at Journal of the American Chemical Society on December 2nd, 2021. See the published version at <https://doi.org/10.1021/jacs.1c09741>.



1 **Phenylboronic acid modification augments the lysosome escape and**  
2 **antitumor efficacy of a cylindrical polymer brush-based prodrug**

3 Ruonan Wang, Changfeng Yin, Changren Liu, Ying Sun, Panpan Xiao, Jia Li, Shuo  
4 Yang, Wei Wu\* and Xiqun Jiang

5 Department of Polymer Science & Engineering, College of Chemistry & Chemical  
6 Engineering, Nanjing University, Nanjing 210023, P. R. China

7

8 \* To whom correspondence should be addressed.

9 E-mail: [wuwei@nju.edu.cn](mailto:wuwei@nju.edu.cn)

10

11

12

13

14

15

16

17

18

19

20

21

22

23 **Abstract**

24 Timely lysosome escape is very important for nanomedicines to avoid premature  
25 degradation. Herein, we report an exciting finding that phenylboronic acid (PBA)  
26 modification can greatly facilitate the lysosome escape of cylindrical polymer brushes  
27 (CPBs), and further promote their exocytosis and transcellular transfer. This  
28 fundamental finding for the first time reveals that PBA groups improve the tumor  
29 penetration of nanomaterials via an active transcytosis mechanism. We speculate that  
30 the mechanism of the PBA-enhanced lysosome escape is associated with the specific  
31 interactions of the PBA group with the lysosomal membrane proteins and hot shock  
32 proteins. The featured advantage of the PBA modification over the known lysosome  
33 escape strategies is that it does not cause significant adverse effects on the properties of  
34 the CPBs. Furthermore, doxorubicin was conjugated to the PBA-modified CPBs with  
35 drug loading content larger than 20%. This CPBs-based prodrug could eradicate the  
36 tumors established in mice by multiple intravenous administration.

37

38

39

40

41

42

43

44

45 Well-designed nano drug delivery systems can selectively accumulate in tumors via  
46 the enhanced permeability and retention (EPR) effect<sup>1-8</sup>. However, they would be in  
47 risk of degradation after cellular internalization and subsequent lysosomal sequestration  
48 because of the hydrolytic enzymes and harsh acidic condition inside the lysosome. Thus,  
49 lysosomal entrapment is a major bottleneck for efficient delivery of therapeutic agents  
50 in subcellular level<sup>6,9-11</sup>. It is crucial for nano carriers to take their cargoes out of  
51 lysosomes in time to avoid the drug degradation and inactivation.

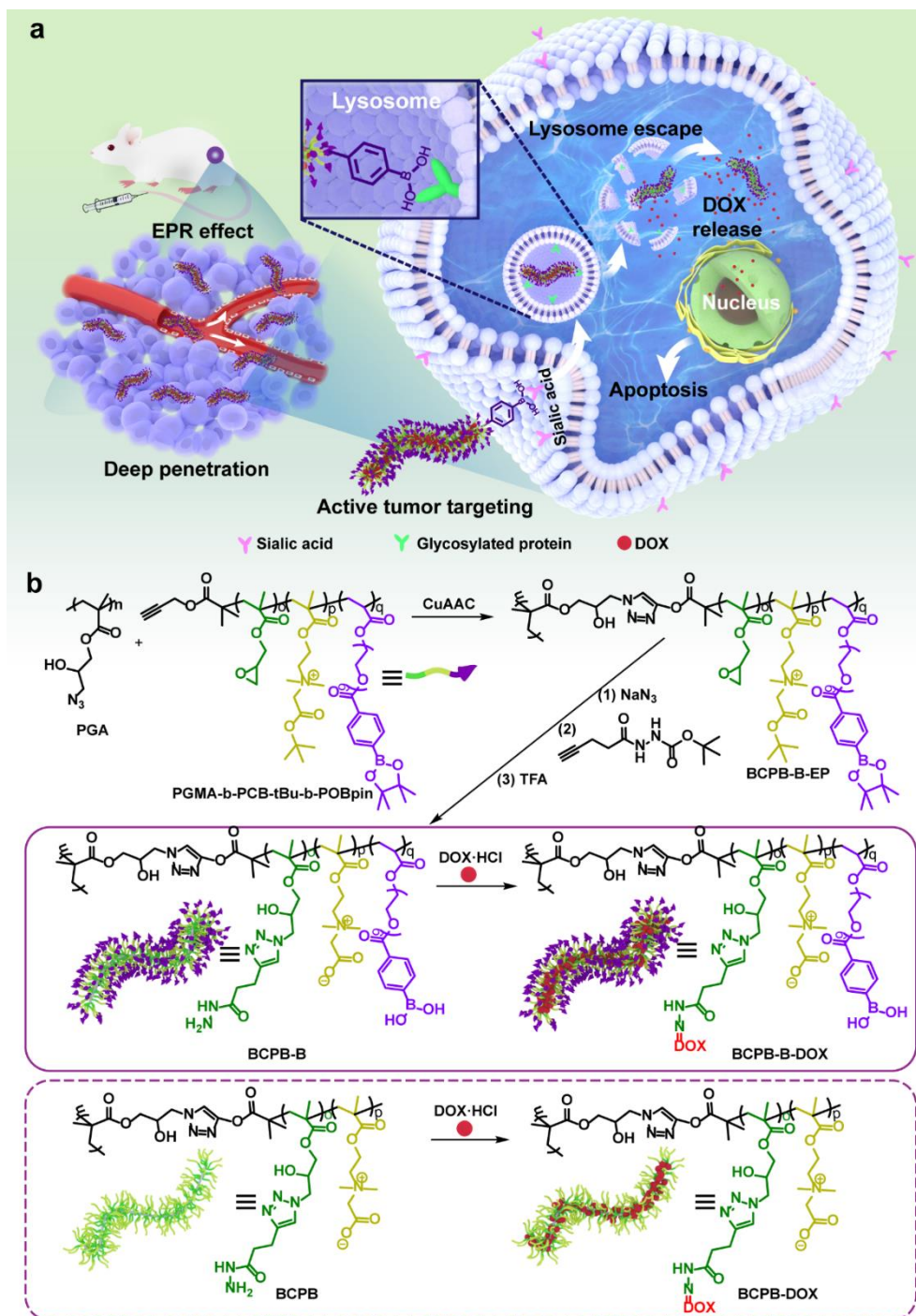
52 Up to now, several approaches have been developed to facilitate the lysosome escape  
53 of nanomaterials<sup>12,13</sup>. For example, by exerting the negative charge state of the  
54 lysosomal membrane, some positively charged materials have been used as drug  
55 carriers and achieve lysosome escape by destabilizing the lysosomal membrane through  
56 electrostatic interactions<sup>14-16</sup>. Another approach involves the materials with  
57 exceptionally abundant basic groups, such as poly(ethylene imine) (PEI). They are used  
58 to rupture lysosomes via the so-called “proton sponge effect”<sup>17-20</sup>. Moreover, membrane  
59 fusion is also an operational way for lysosome escape, which can be accomplished by  
60 using cationic liposomes or fusogenic peptides. The former fuses with the lysosome  
61 membrane via electrostatic interactions, and the fusogenic peptides achieve membrane  
62 fusion through conformational change in the acidic condition of lysosomes<sup>21-24</sup>. The  
63 approach termed as photochemical internalization (PCI) achieves lysosome escape via  
64 photosensitizers that yield reactive oxygen species (ROS) under illumination and  
65 further induce lysosome rupture through the damage effect of ROS<sup>25-29</sup>. Although the  
66 approaches mentioned above can achieve lysosome escape, they have respective

67 noticeable drawbacks. As well documented, after intravenous injection, the positively  
68 charged materials are prone to opsonization and hence have short blood circulation and  
69 little opportunity to reach tumors<sup>4,6,30</sup>. The strategy of charge reversal can keep the  
70 materials neutral or anionic in blood circulation and trigger cationization at disease sites,  
71 however, sophisticated design and preparation are needed and the efficient charge  
72 reversal at the target sites is still a huge challenge<sup>31</sup>. For the case of fusogenic peptides,  
73 their ability to escape from lysosomes would be diminished after conjugation to  
74 nanomaterials, and their high cost and quite complicated preparation may also limit  
75 greatly their applications<sup>32</sup>. The PCI approach is greatly limited by the low tissue  
76 penetration depth of the exciting light and thus only applicable to superficial tumors,  
77 and introducing photosensitizers may cause additional toxicity<sup>33-35</sup>. Accordingly,  
78 developing effective strategy for the lysosome escape of nanomaterials without adverse  
79 effects on other performances is very important for tumor therapy.

80 Herein, we present an exciting finding that phenylboronic acid (PBA) modification  
81 can greatly facilitate the lysosome escape of cylindrical polymer brushes (CPBs), and  
82 further promote their exocytosis and transcellular transfer. In published studies, it has  
83 been frequently observed that PBA groups can augment significantly the tumor  
84 targeting ability of nanomaterials through the specific interaction with the sialic acid  
85 (SA) residues overexpressed on various tumor cells and concomitantly enhance their  
86 tumor penetration<sup>36-38</sup>. However, the mechanism for enhancing tumor penetration is still  
87 unclear. This work demonstrates that it is an active transcytosis process relying on the  
88 PBA-mediated cellular uptake, and PBA-enhanced lysosome escape and exocytosis.

89 Furthermore, using the PBA-modified CPBs as nano carriers, we incorporated  
90 doxorubicin (DOX) through pH-sensitive acylhydrazone linkage, and achieved high  
91 drug loading content larger than 20% and high tumor therapeutic efficacy. CPBs are a  
92 class of nanoscale one-dimensional polymers with wormlike morphology. This  
93 morphology together with their well-defined chemical structure and controllable size  
94 make them very suitable for delivering drugs, because the wormlike morphology is  
95 favorable to tumor penetration and well-controlled chemical structure and size provide  
96 reproducible pharmacokinetic and pharmacological profiles<sup>39,40</sup>. The PBA-modified  
97 CPBs designed here also have several other advantages, including 1) the PBA groups  
98 can not only promote the lysosome escape but also augment the tumor targeting ability  
99 and tumor permeability of the CPBs as illustrated in Fig. 1a; 2) the zwitterionic  
100 poly(carboxybetaine) (PCB) block in the side chains provide high water solubility and  
101 high anti-biofouling ability<sup>41-43</sup>; 3) the inner poly(glycidyl methacrylate) (PGMA)  
102 block in the side chains provide sufficient modification sites and high drug loading.  
103 These superiorities enable the prodrug to eradicate the tumors established in mice after  
104 multiple intravenous administration.

105



106

107 **Fig. 1 Biological functions and synthesis and of the CPBs. a** Illustration of the tumor

108 targeting and lysosome escape of BCPB-B-DOX. The abundant PBA groups of BCPB-

109 B-DOX is conducive to tumor targeting and lysosome escape, and can greatly improve

110 the antitumor efficacy of the prodrug. **b** Synthesis and drug loading of the CPBs.

111

## 112 Results

113 **Syntheses and characterizations of the drug-loaded polymer brushes.** To make  
114 clear the effect of PBA modification on the lysosome escape of CPBs and achieve  
115 efficient tumor therapy, we meticulously designed the water-soluble PBA-modified  
116 CPBs (named BCPB-B) as well as PBA-free CPBs (named BCPB) as reference  
117 materials. Their chemical structures and synthesis routes can be found in Fig. 1b. The  
118 backbone (named PGA, Fig. 1b) of BCPB-B and BCPB was synthesized by  
119 polymerizing the monomer glycidyl methacrylate via reversible addition-fragmentation  
120 chain transfer (RAFT) polymerization (giving PGMA), followed by converting the  
121 epoxy groups to azido groups via the reaction with sodium azide (Supplementary  
122 Scheme 1). The side chain of BCPB-B is a triblock copolymer and synthesized by a  
123 three-step atom transfer radical polymerization (ATRP) with propargyl 2-  
124 bromoisobutyrate as an initiator (Supplementary Scheme 1). The inner block (the block  
125 adjacent to the backbone) of the side chain is designed to be PGMA, whose abundant  
126 epoxy side groups can be used for functionalizations. The second block is poly(2-  
127 tertbutoxy-*N*-(2-(methacryloyloxy)ethyl)-*N,N*-dimethyl-2-oxoethanaminium) (PCB-  
128 tBu). After the cleavage of the *tert*-butyl ester protecting groups, a zwitterionic  
129 poly(carboxybetaine) (PCB) block can be formed and impart high water solubility and  
130 anti-biofouling ability. The third block is poly(OEGMA-Bpin) (POBpin,  
131 Supplementary Scheme 1) and is used to provide PBA functional groups after removing  
132 the pinacol ester. The reference material BCPB has the side chains without the third  
133 block, which is the only difference comparing to BCPB-B. For both the two types of

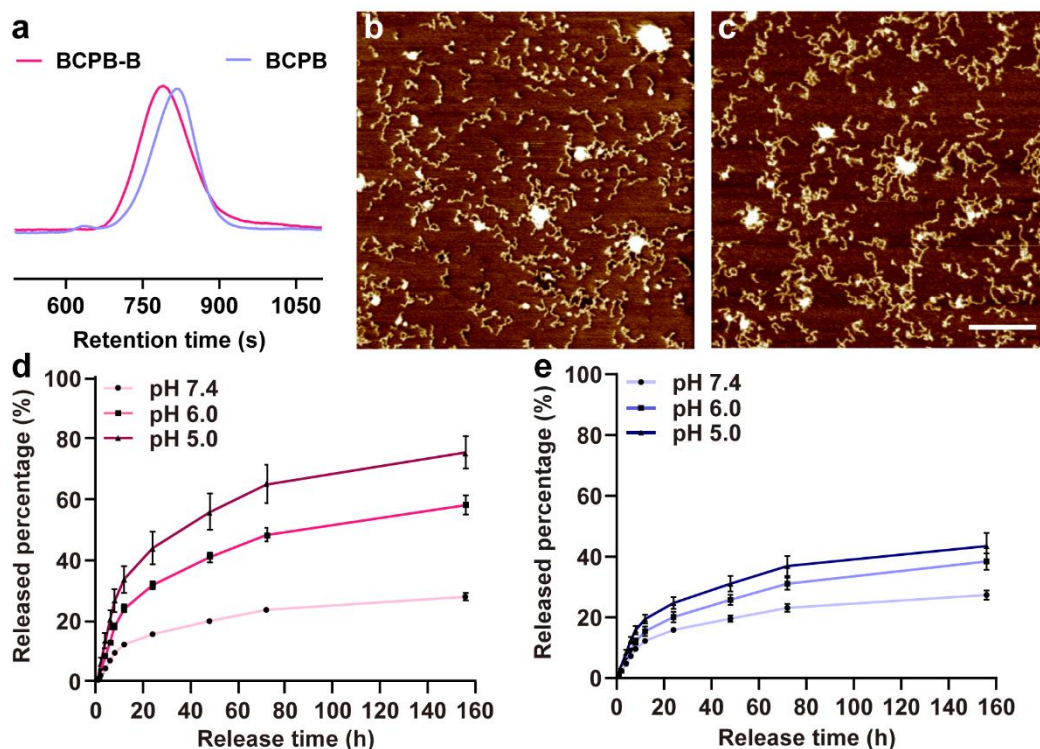
134 CPBs, the side chains were grafted onto the backbones through the Cu(I)-  
135 catalyzed alkyne-azide 1,3-dipolar cycloaddition (CuAAC). Antitumor agent DOX was  
136 covalently bound to the PGMA block of BCPB-B and BCPB through a pH-sensitive  
137 acylhydrazone linkage to achieve the responsive drug release in the weak acid  
138 environment of tumors. We take BCPB-B as an example to illustrate the drug loading  
139 process. We first converted the epoxy groups in BCPB-B-EP (Fig. 1b) to azido groups  
140 through the reaction with sodium azide, and then performed the CuAAC between the  
141 azido groups and *N*-propynoyl-hydrazinecarboxylic acid *tert*-butyl ester (PHTE),  
142 affording BCPB-B-Boc (Supplementary Scheme 1). After the cleavage of the *tert*-  
143 butyloxycarbonyl (Boc) protecting groups by trifluoroacetic acid (TFA), acylhydrazine  
144 side groups were formed in the inner block and used to link DOX via the reaction with  
145 the carbonyl group in DOX. It is notable that in the process of the Boc cleavage, the  
146 protecting groups of the *tert*-butyl ester in the second block and the pinacol ester in the  
147 third block would also be completely cleaved, affording BCPB-B (Fig. 1b). The DOX-  
148 loaded BCPB-B and BCPB are named BCPB-B-DOX and BCPB-DOX (Fig. 1b),  
149 respectively.

150 The characterization data of BCPB-B-DOX and BCPB-DOX as well as their  
151 precursors can be found in Supplementary Fig. 1-18. The <sup>1</sup>H NMR spectrum of the  
152 backbone PGA is compared with that of PGMA in Supplementary Fig. 1. As can be  
153 seen, the proton signals of the glycidyl moieties are observed at 3.23, 2.84, and 2.64  
154 ppm in the spectrum of PGMA, and disappear completely in the spectrum of PGA,  
155 indicating the high conversion efficiency of the epoxy to azido group. The number

156 average molecular weight ( $M_n$ ) and polydispersity indexes ( $D$ ) of PGMA were  
157 measured to be ~147,000 and 1.13 by gel permeation chromatography (GPC),  
158 respectively (Supplementary Fig. 2). The narrowly distributed molecular weight of the  
159 backbone would provide the polymer brushes with narrowly distributed length. To  
160 minimize the confounding factors, we used the second-step ATRP product of the side  
161 chain of BCPB-B as the side chain of BCPB. The side chain of BCPB-B and its  
162 precursors were structurally characterized by  $^1\text{H}$  NMR spectra as shown in  
163 Supplementary Fig. 4-6. The polymerization degrees of the PGMA, PCB-tBu and  
164 POBpin blocks were estimated to be about 27, 55 and 12 by the  $^1\text{H}$  NMR spectra,  
165 respectively. The GPC data of the three-step ATRP products PGMA, PGMA-PCB-tBu  
166 and PGMA-PCB-tBu-POBpin are shown in Supplementary Fig. 7. Their  $M_n$  and  $D$   
167 values are determined to be 11705/1.17, 18397/1.23, and 23418/1.28, respectively.  
168 After grafting the side chains onto the backbone, we obtained the polymer brushes  
169 BCPB-B-EP and BCPB-EP. The high grafting efficiencies are evidenced by the  
170 comparison of the Fourier transform infrared (FTIR) spectra of the backbone and the  
171 polymer brushes. As shown in Supplementary Fig. 18, a strong absorption band at 2100  
172  $\text{cm}^{-1}$  assigned to the azido groups can be observed in the FTIR spectrum of PGA and  
173 disappears completely in the spectra of the polymer brushes, indicating that almost all  
174 the azido groups have reacted with the alkynyl end group of the side chain. We also  
175 checked the size distributions of BCPB-B-EP and BCPB-EP by GPC measurements,  
176 although the measurements can not provide accurate molecular weight information of  
177 the polymer brushes due to the huge structural difference between the brushes and the

178 linear polystyrene standards (Fig. 2a). Unimodal molecular weight distributions were  
179 observed for both BCPB-B-EP and BCPB-EP with  $D$  values of about 1.29 and 1.26.  
180 The narrowly distributed sizes are greatly favorable for identifying the differences in  
181 biological properties caused by the chemical structure, since the interference resulting  
182 from different sizes can be essentially excluded. As stated above, DOX is conjugated  
183 to the polymer brushes through the pH-sensitive acylhydrazone linkage, affording  
184 BCPB-B-DOX and BCPB-DOX. The aromatic proton signals from the DOX moieties  
185 can be observed at 8.10-7.60 ppm in their  $^1\text{H}$  NMR spectra (Supplementary Fig. 16-17).  
186 The UV-vis absorption spectra of BCPB-B-DOX, BCPB-DOX and DOX are shown in  
187 Supplementary Fig. 19a. It can be seen that both BCPB-B-DOX and BCPB-DOX have  
188 the absorption characteristics of DOX. The DOX contents of BCPB-B-DOX and  
189 BCPB-DOX were determined by measuring the absorbance at 489 nm with a pre-  
190 established calibration curve. Thanks to the abundant reaction sites, BCPB-B-DOX and  
191 BCPB-DOX present high DOX contents of about 21% and 23%, respectively, and  
192 maintain desirable water solubility as shown by the photograph of their water solutions  
193 (Supplementary Fig. 19b).

194



195

196 **Fig. 1 Characterizations and drug release behaviors of the polymer brushes. a** GPC

197 curves of BCPB-B and BCPB. **b,c** Typical AFM height images of BCPB-B (**b**) and

198 BCPB (**c**) adsorbed on freshly cleaved mica from dilute water solutions. Scale bars =

199 200 nm. **d,e** In vitro DOX release profiles of BCPB-B-DOX (**d**) and BCPB-DOX (**e**)

200 in PBS (0.01 M) with different pH values at 37 °C.

201 We examined the morphological structures of the two types of polymer brushes

202 before and after drug loading by atomic force microscopy (AFM). As shown in Fig. 2b,

203 c, both BCPB-B and BCPB have a typical one-dimensional wormlike morphology with

204 an average length of ~90 nm and cross sectional diameter of ~18 nm. The various

205 instantaneous configurations of the polymer brushes shown in the AFM images indicate

206 their good flexibility. From the AFM images of BCPB-B-DOX and BCPB-DOX

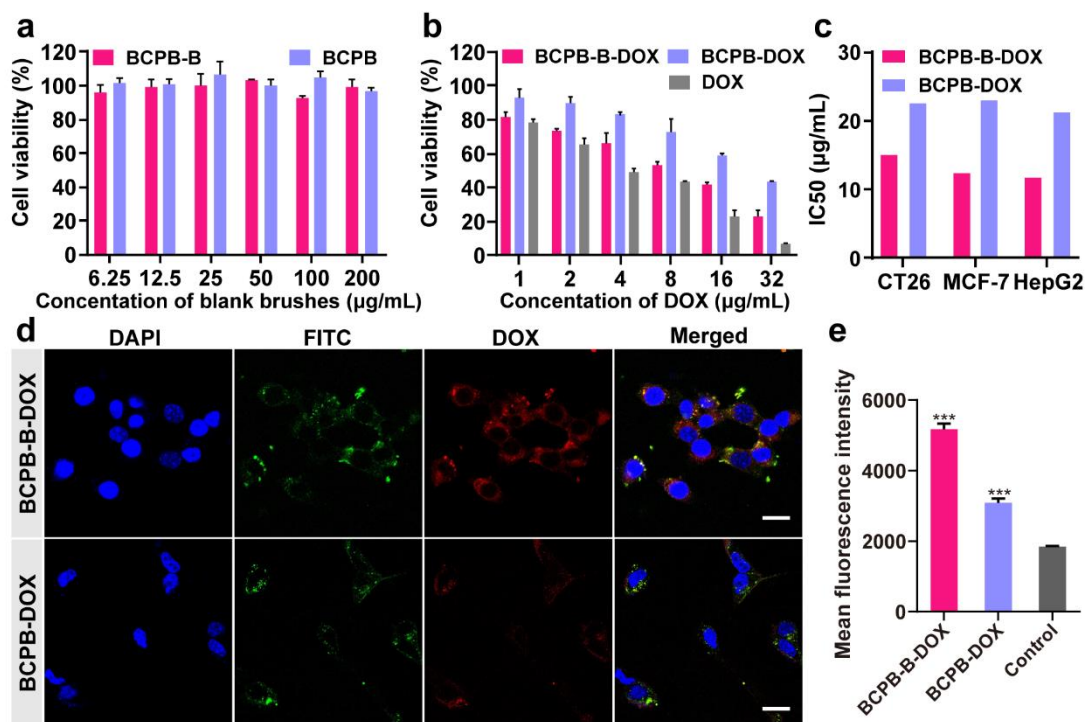
207 (Supplementary Fig. 19c, d), it can be seen that the morphologies of the polymer

208 brushes do not change significantly after the drug loading.

209 **In vitro drug release.** We studied the in vitro DOX release profiles of BCPB-B-DOX  
210 and BCPB-DOX in different pH media simulating the physiological environments of  
211 blood circulation (pH ~7.4), tumors (pH 6.5–6.0), and lysosomes (pH 4.5–5.5),  
212 respectively. As shown in Fig. 2d, e, typical pH-dependent release behaviors are  
213 observed for both BCPB-B-DOX and BCPB-DOX. At pH 7.4, there are only  $27.9 \pm$   
214  $1.1\%$  and  $27.3 \pm 1.5\%$  of DOX released within 156 h for BCPB-B-DOX and BCPB-  
215 DOX, respectively. As expected, with the decrease of pH, the drug release rates of the  
216 two samples increase remarkably. At pH 6.0, the cumulative release percentages within  
217 156 h are  $58.1 \pm 3.2\%$  for BCPB-B-DOX and  $38.4 \pm 2.7\%$  for BCPB-DOX, and at pH  
218 5.0, the values are  $75.5 \pm 5.6\%$  and  $43.5 \pm 4.4\%$ , respectively. It is notable that the drug  
219 release rate of BCPB-B-DOX is significantly higher than that of BCPB-DOX in the  
220 same conditions. We speculate that in BCPB-DOX, the strong dipole-dipole  
221 interactions between the zwitterionic PCB repeating units make the PCB segments  
222 packed closely, hindering greatly the DOX release from the inner block, by contrast, in  
223 BCPB-B-DOX, the third block may disrupt the closely packing of the zwitterionic PCB  
224 segments in some extent, leading to the faster drug release<sup>44</sup>. The pH-sensitive drug  
225 release behaviors of BCPB-B-DOX and BCPB-DOX are attributable to the  
226 acylhydrazone linkage between the DOX and polymer brush moieties, and are greatly  
227 beneficial for reducing unwanted side effects and enhancing therapy efficacy since the  
228 drug release in circulatory system is remarkably limited and tumor-specific release is  
229 basically achieved.

230  
231

232 **In vitro cytotoxicity and cellular uptake.** To evaluate the pharmacological activity of  
233 the drug-loaded polymer brushes and the biosafety of the drug-free polymer brushes, the  
234 cytotoxicities of BCPB-B-DOX and BCPB-DOX against mouse colon carcinoma cells  
235 (CT26), human breast cancer cells (MCF-7) and human liver tumor cells (HepG2) were  
236 measured by MTT assay with BCPB-B and BCPB as negative control and DOX as  
237 positive control. For all the three cell lines, the blank brushes do not show significant  
238 cytotoxicity even at a high concentration of 200  $\mu\text{g/mL}$ , indicating their good  
239 cytocompatibility (Fig. 3a, Supplementary Fig. 20). By contrast, each of the three DOX  
240 formulations of BCPB-B-DOX, BCPB-DOX and free DOX displays a dose-dependent  
241 cytotoxicity, and the former two show slightly lower anti-proliferation efficiency than  
242 free DOX, which can be ascribed to the sustained release behaviors of BCPB-B-DOX  
243 and BCPB-DOX (Fig. 3b, Supplementary Fig. 21). The  $\text{IC}_{50}$  values of the three DOX  
244 formulations against the three cell lines were calculated and compared in Fig. 3c.  
245 Notably, for each cell line, BCPB-B-DOX shows a much lower  $\text{IC}_{50}$  than BCPB-DOX,  
246 which is attributable to the PBA groups in BCPB-B-DOX that can promote the cellular  
247 uptake due to the targeting effect of the PBA groups on the SA-positive cells.



248

249 **Fig. 2 In vitro cytotoxicity and cellular uptake of the polymer brushes. a,b** MTT  
 250 assays for blank brushes (a) and drug-loaded brushes (b) against CT26 cells after 24 h  
 251 incubation. c IC50 calculated from MTT assay data. d,e CLSM images (d) and mean  
 252 fluorescence intensity measured by flow cytometry (e) of the CT26 cells after 2 h  
 253 incubation with the FITC-labeled BCPB-B-DOX and BCPB-DOX at 37 °C,  
 254 respectively. Scale bars = 20 µm. \* $P < 0.05$ , \*\* $P < 0.01$ , \*\*\* $P < 0.001$  compared with  
 255 control.

256 We further studied the cellular uptake behaviors of BCPB-B-DOX and BCPB-DOX  
 257 qualitatively and quantitatively by confocal laser scanning microscopy (CLSM) and  
 258 flow cytometry after labeling them with fluorescein isothiocyanate (FITC) through the  
 259 reaction of the residue acylhydrazine groups in the polymer brushes with the  
 260 isothiocyanate group in the dye. As shown in Fig. 3d and Supplementary Fig. 22 after  
 261 2 h incubation, bright signals from FITC and DOX are observed in all the CT26, MCF-

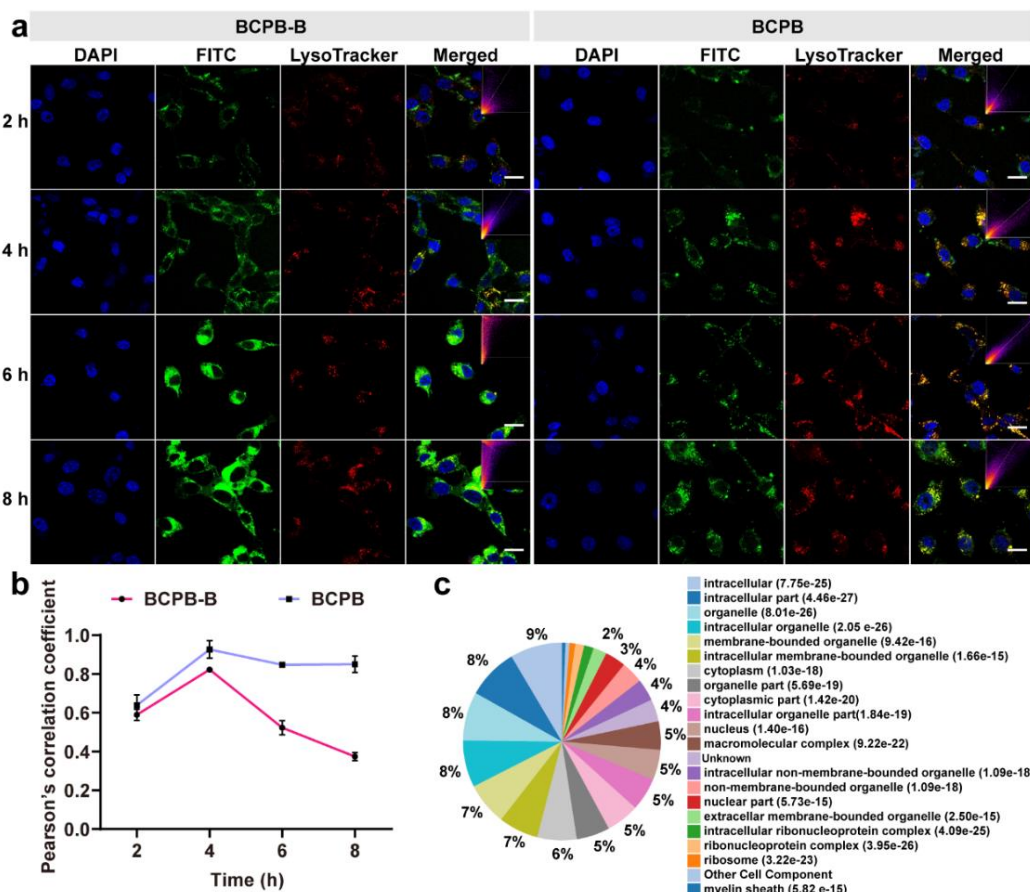
262 7 and HepG2 cells incubated with BCPB-B-DOX and BCPB-DOX, respectively. The  
263 internalized samples are mainly distributed in the cytoplasm in a punctate pattern,  
264 indicating that endocytosis may play a major role in the cellular uptake of the samples.  
265 For all the three cell lines, it can be seen that the fluorescence signals from both FITC  
266 and DOX in the cells treated with BCPB-B-DOX are significantly stronger than those  
267 in the cells treated with BCPB-DOX, which is confirmed by the flow cytometry  
268 quantitative analyses. As shown in Fig. 3e and Supplementary Fig. 22 the mean  
269 fluorescence intensities in the CT26, MCF-7 and HepG2 cells incubated with BCPB-  
270 B-DOX are 1.67-fold, 2.67-fold, and 2.58-fold the intensities in the corresponding cells  
271 treated with BCPB-DOX, respectively, which can be attributed to the targeting effect  
272 of the PBA group. The effect degree of the PBA group on the cellular uptake is  
273 positively related with the SA expression level of the cells, hence the cellular uptake  
274 results are consistent well with the fact that MCF-7 cells have the highest SA level  
275 among the three cell lines<sup>37,45</sup>. The higher cellular uptake of BCPB-B-DOX than BCPB-  
276 DOX also explains its lower IC<sub>50</sub> in the three cell lines.

277 **Lysosome escape.** Timely lysosome escape is very important for preserving the  
278 pharmacological activity of the endocytosed nanomedicines. We investigated the  
279 lysosome escape behaviors of the FITC-labeled BCPB-B and BCPB by fluorescence  
280 co-localization of the labeled brushes and LysoTracker red in CT26 cells via CLSM  
281 imaging and by Pearson co-localization analyses to quantify the escape rate (Fig. 4a, b).  
282 The Pearson's correlation coefficients between the green signals from the FITC-labeled  
283 CPBs and the red signals from LysoTracker as a function of incubation time are shown

284 in Fig. 4b. It can be seen that for both BCPB-B and BCPB, the coefficients at 4 h post-  
285 treatment are larger than those at 2 h, probably because at 2 h, the CPBs have not been  
286 adequately internalized by the cells yet. When the incubation time is prolonged from 4  
287 h to 8 h, for BCPB, the coefficient only decreases slightly from 0.93 to 0.85, by contrast,  
288 for BCPB-B, the coefficient decreases dramatically from 0.82 to 0.37, revealing that  
289 the lysosome escape rate of BCPB-B is much higher than that of BCPB in the same  
290 condition. To confirm the higher lysosome escape ability of BCPB-B, we further  
291 examined the lysosome escape behaviors of BCPB-B and BCPB in MCF-7 and HepG2  
292 cell lines and obtained similar results (Supplementary Fig. 23). It is worth noting that  
293 for all the three cell lines, at each time point, the Pearson's correlation coefficient of  
294 BCPB-B is lower than that of BCPB, probably because the lysosome escape of BCPB-  
295 B occurs very soon after entering lysosomes.

296 To explore the mechanism of the PBA-enhanced lysosome escape, we conjugated  
297 alkynyl-bearing  $\text{Fe}_3\text{O}_4$  nanoparticles (the diameter is  $\sim 10$  nm) to BCPB-B- $\text{N}_3$  and  
298 BCPB- $\text{N}_3$  via CuAAC. After incubated with CT26, MCF-7 and HepG2 cells for 12 h,  
299 respectively, the  $\text{Fe}_3\text{O}_4$ -modified BCPB-B and BCPB together with the adsorbed  
300 proteins were isolated via magnetic separation technique. The proteins adsorbed  
301 specifically by the  $\text{Fe}_3\text{O}_4$ -modified BCPB-B and BCPB were collected and identified  
302 by GeneOntology (GO) pathway Cellular Component (CC) analysis (Fig. 4c,  
303 Supplementary Fig. 24, Supplementary Table 1, 2). It is found that in all three cell lines,  
304 comparing to BCPB, BCPB-B uniquely adsorbs lysosomal membrane proteins and hot  
305 shock proteins (HSPs). The unique protein adsorption behavior of BCPB-B is

306 ascribable to the specific interactions of the PBA groups in BCPB-B with the glycosyl  
 307 and basic groups, such as amino or guanidine group, in the proteins. We surmise that  
 308 the lysosomal membrane proteins adsorbed by BCPB-B may play a mediation role in  
 309 the lysosome escape of BCPB-B. In addition, it is notable that among the HSPs  
 310 adsorbed by BCPB-B, Hsp90 is a crucial regulator of vesicular transport of cellular  
 311 cargo<sup>46</sup>, and Hsp70 is a survival protein directly related to endo-lysosomal compartment  
 312 and maintains the integrity of lysosome by preventing membrane permeabilization<sup>47,48</sup>.  
 313 Accordingly, we speculated that the PBA-enhanced lysosome escape may also be  
 314 associated with the adsorption of the HSPs.



315

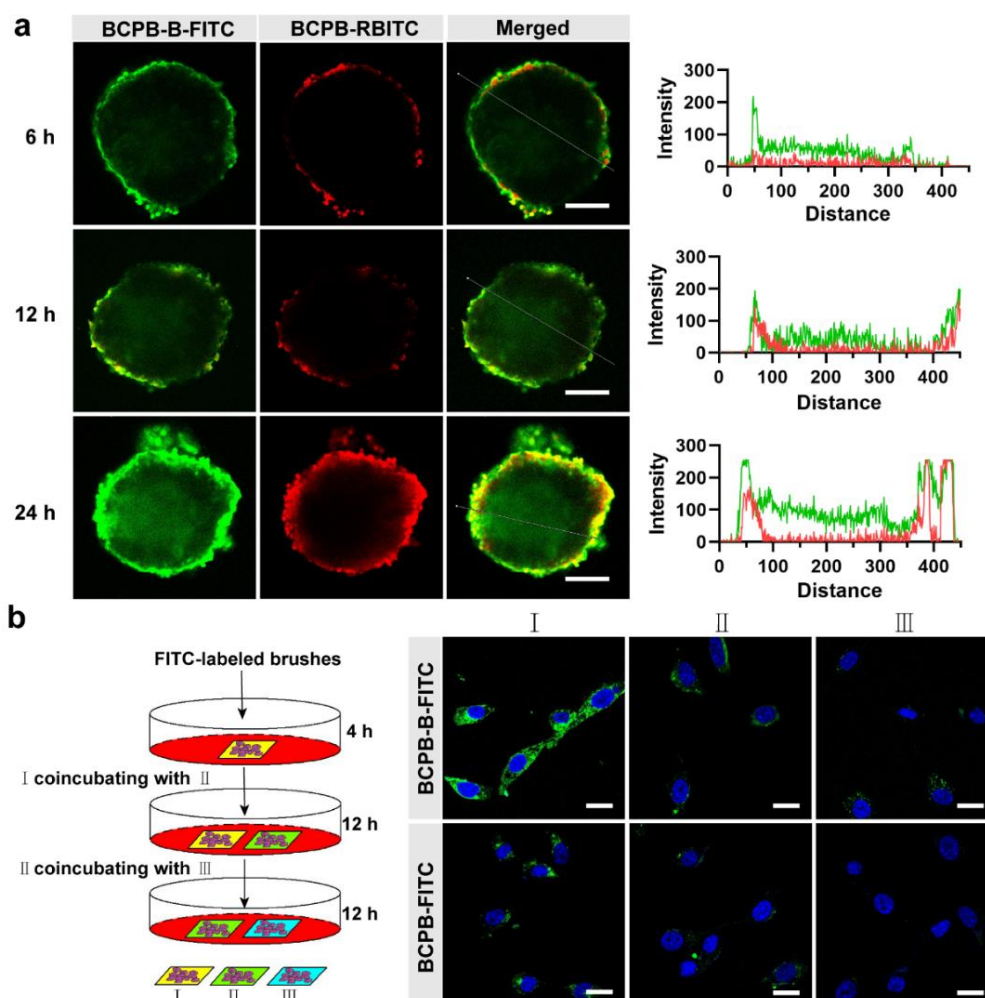
316 **Fig. 3 Lysosome escape behaviors of BCPB-B and BCPB.** a Co-localization

317 observation by CLSM of the FITC-labeled brushes (green) and LysoTracker (red) in

318 CT26 cells. Scale bars = 20  $\mu\text{m}$ . **b** Evolution with time of the Pearson's correlation  
319 coefficients between the signals from the FITC-labeled CPBs and LysoTracker. **c**  
320 GeneOntology (GO) pathway Cellular Component (CC) analysis of BCPB-B in CT26  
321 cells.

322 **Penetration in multicellular spheroids (MCs).** High tumor permeability of  
323 nanomedicines enables them to penetrate in avascular regions and hence can improve  
324 significantly their treatment effect. We studied the permeabilities of BCPB-B and  
325 BCPB in MCs to simulate and evaluate their tumor penetration. Two different MCs  
326 prepared from HepG2 and CT26 cells were used. To clearly compare the permeabilities  
327 of BCPB-B and BCPB, we labeled them with two different dyes FITC and rhodamine  
328 B isothiocyanate (RBITC), respectively, treated MCs with the FITC-labeled BCPB-B  
329 and RBITC-labeled BCPB together for different periods, and observed the incubated  
330 MCs by CLSM. As shown in Fig. 5a and Supplementary Fig. 25, both the labeled  
331 BCPB-B and BCPB exhibit time-dependent penetration behaviors in HepG2 MCs.  
332 After 6 h incubation, the FITC-labeled BCPB-B already penetrated to the center of the  
333 MCs, whereas, the RBITC-labeled BCPB penetrated very little. As time goes by, more  
334 BCPB-B and BCPB penetrated into the MCs. At 24 h post-treatment, bright green  
335 signals from BCPB-B are observed in the center of the MCs, whereas, the penetration  
336 depth of BCPB is only about 50  $\mu\text{m}$ . The different permeabilities of BCPB-B and BCPB  
337 are also clearly reflected by the fluorescence plate quantification data of the MCs (Fig.  
338 5a). The relatively higher permeability of BCPB-B was confirmed in CT26 MCs  
339 (Supplementary Fig. 26 and 27). Due to the lower SA level of CT26 cells than HepG2

340 cells, the penetration depth of BCPB-B in CT26 MCs is lower than that in HepG2 MCs,  
 341 nevertheless, the penetration of BCPB in CT26 MCs is comparable to that in HepG2  
 342 MCs, which further proves the role of the PBA group in the penetration of BCPB-B.



343  
 344 **Fig. 4 Penetration behaviors of BCPB-B and BCPB in MCs. a** CLSM images of the  
 345 optical slices through the centers of HepG2 MCs incubated jointly with the FITC-  
 346 labeled BCPB-B and RBITC-labeled BCPB for different periods (left) and the  
 347 corresponding fluorescence plate quantification data of the MCs (right). Scale bars =  
 348 100  $\mu$ m. **b** Transcellular transfer study of the FITC-labeled BCPB-B and BCPB in CT26  
 349 cells. The left diagram illustrates the general experimental procedures. The cells on  
 350 coverslips (I) were coincubated with the FITC-labeled CPBs for 4 h, washed with PBS

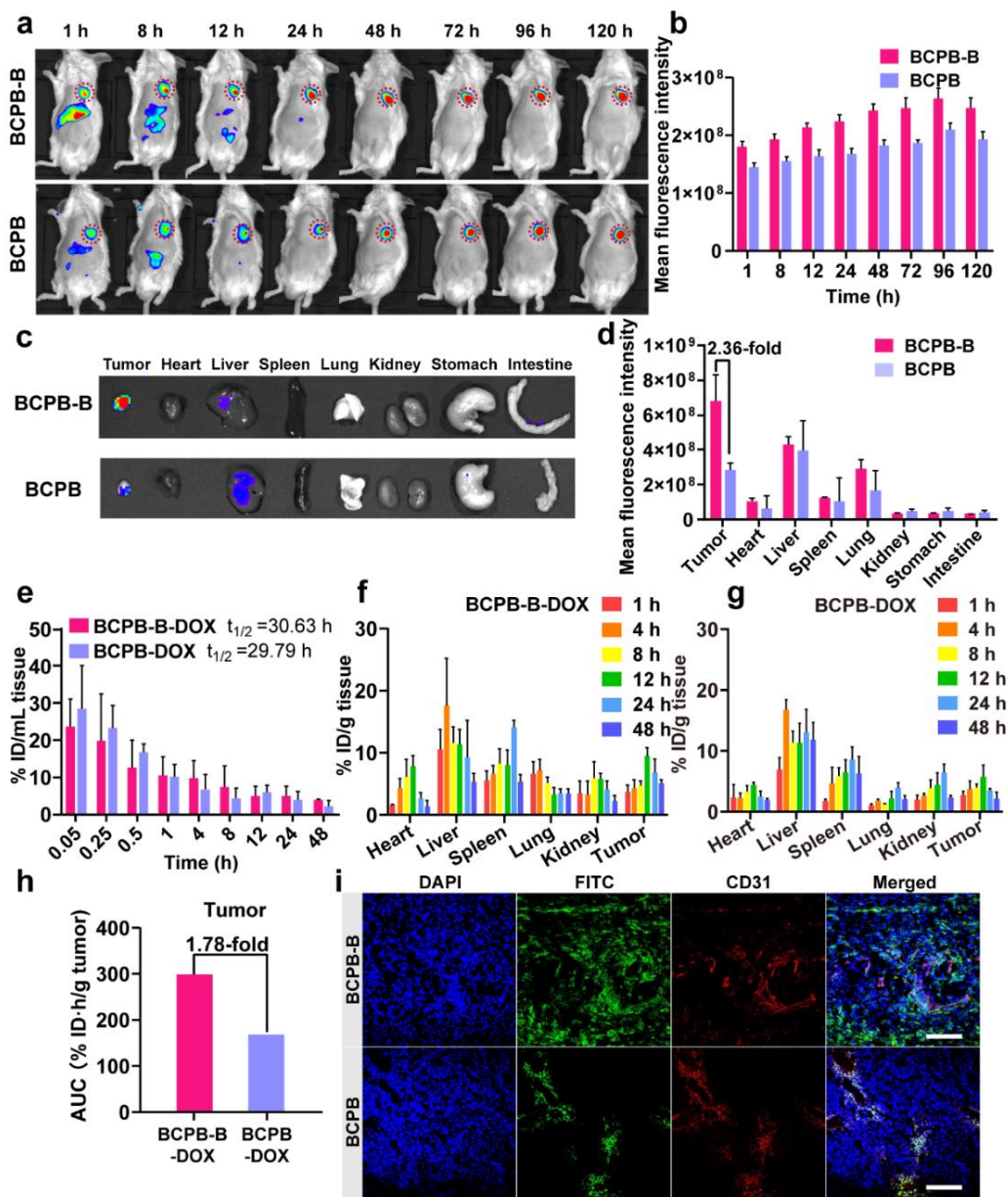
351 and imaged by CLSM. Thereafter, the coverslips (I) were coincubated with coverslips  
352 (II) bearing fresh cells in fresh culture medium for 12 h. After repeating the above  
353 process, coverslips (III) were obtained. The right picture shows the CLSM images of  
354 the cells on the coverslips (I), (II) and (III), respectively. Scale bars = 20  $\mu\text{m}$ .

355 **In vitro transcellular transfer.** We surmise that the higher permeability of BCPB-B in  
356 MCs may be associated with the PBA-enhanced lysosome escape. After escaping from  
357 lysosomes, BCPB-B may further achieve efficient transcytosis by repeating exocytosis,  
358 PBA-augmented cellular uptake and PBA-accelerated lysosome escape. To verify this  
359 hypothesis, we studied the transcellular transfer of BCPB-B and BCPB among different  
360 batches of CT26 cells by CLSM observations, respectively. As illustrated by the left  
361 diagram in Fig. 5b, the cells on coverslips (I) were first coincubated with the FITC-  
362 labeled CPBs for 4 h, and then washed with PBS and observed representatively by  
363 CLSM. Thereafter, the coverslips (I) were further coincubated with coverslips (II)  
364 bearing fresh cells in fresh culture medium for 12 h. After repeating the above process,  
365 we also obtained coverslips (III). In doing so, the transfer of BCPB-B and BCPB among  
366 the cells on the coverslips (I), (II) and (III) can be compared clearly. From the typical  
367 CLSM images shown in Fig. 5b, it can be seen that the signals from BCPB-B in the  
368 cells of the coverslips (I), (II) and (III) are significantly higher than the signals from  
369 BCPB in the cells of corresponding coverslips, indicating that for BCPB-B, the  
370 processes of cellular uptake, exocytosis and subsequent transcellular transfer are faster  
371 than the case of BCPB. The faster cellular uptake of BCPB-B is attributable to the  
372 targeting effect of the PBA groups, and the faster exocytosis should result from the

373 PBA-enhanced lysosome escape, which jointly facilitated the transcellular transport  
374 and also the penetration of BCPB-B in MCs. Similar results were obtained by using  
375 CT26 and MCF-7 cells (Supplementary Fig. 28).

376 **In vivo near infrared fluorescence (NIRF) Imaging.** To gain insight into the nano-  
377 bio interactions in a living body, we traced the in vivo behaviors of BCPB-B-DOX and  
378 BCPB-DOX by NIRF imaging after labeling them with a near infrared dye NIR-797,  
379 and injecting the labeled samples into subcutaneous hepatic H22 tumor-bearing mice  
380 via tail vein. As shown in Fig. 6a, the signals from BCPB-B-DOX and BCPB-DOX can  
381 be observed in the tumors, livers and intestines during 1-12 h postinjection (p.i.). As  
382 time elapsed, the signals in tumors increase and those in normal tissues decrease. At 96  
383 h p.i., the signal intensities of BCPB-B-DOX and BCPB-DOX in tumors reach their  
384 respective maxima, and at each test time point, the signal intensity of BCPB-B-DOX in  
385 tumors is higher than that of BCPB-DOX (Fig. 6b). After finishing the in vivo imaging  
386 at 168 h p.i., we excised and imaged the tumors and main organs for semiquantitative  
387 biodistributions (Fig. 6c, d). Notably, the signal intensity of BCPB-B-DOX in tumors  
388 is about 2.36-fold that of BCPB-DOX, indicating the higher tumor targeting ability of  
389 BCPB-B-DOX than BCPB-DOX, which should be contributed by the PBA-SA specific  
390 recognition.

391



392

393 **Fig. 5 Biodistributions of BCPB-B-DOX and BCPB-DOX in tumor-bearing mice.**

394 **a,b** NIRF images of the H22 tumor-bearing mice (**a**) and mean fluorescence intensities

395 of the tumors (**b**) at different time points after tail-vein injection of the NIR-797-labeled

396 BCPB-B-DOX and BCPB-DOX, respectively. The tumor region is circled by a red

397 dotted line. **c,d** NIRF images (**c**) and mean fluorescence intensities (**d**) of the tumors

398 and organs excised at 168 h after injecting the labeled BCPB-B-DOX and BCPB-DOX.

399 **e** DOX concentrations in plasma versus time after tail-vein injection of BCPB-B-DOX

400 and BCPB-DOX. **f,g** DOX concentrations in different tissues at different time points  
401 after tail-vein injection of BCPB-B-DOX (**f**), and BCPB-DOX (**g**), data are presented  
402 as mean  $\pm$  SD (n = 3). **h** AUC of DOX accumulation in tumors in BCPB-B-DOX and  
403 BCPB-DOX groups. **i** CLSM images of the frozen sections of the tumors from the mice  
404 at 96 h after tail-vein injection of the FITC-labeled BCPB-B and BCPB, respectively.  
405 Scale bars = 100  $\mu$ m.

406 **In vivo drug delivery.** To understand the different properties of BCPB-B and BCPB in  
407 drug delivery, we analyzed quantitatively the DOX distributions in subcutaneous H22  
408 tumor-bearing mice as a function of time after tail-vein injection of BCPB-B-DOX and  
409 BCPB-DOX at a dose of 4 mg/kg DOX equivalent. The DOX concentrations in the  
410 blood, heart, liver, spleen, lung, kidney and tumor were determined by fluorescence  
411 spectroscopy after DOX extraction from the tissue homogenates, respectively. The  
412 evolution with time of the DOX concentrations in blood is shown in Fig. 6e. For both  
413 BCPB-B-DOX and BCPB-DOX, the concentration-time profiles fit well into the two-  
414 compartment model and their elimination half-lives are calculated to be about 29.7 h  
415 and 30.6 h, respectively. As shown in Fig. 6f, g, all the DOX contents in the test organs  
416 and tumor tissues experience a process of growing and then decreasing over time. The  
417 livers and spleens exhibit relatively higher uptake among all the test samples due to the  
418 capture of mononuclear phagocytic system (MPS). For BCPB-B-DOX, the maximal  
419 DOX concentrations in the heart, liver, spleen, lung, and kidney are  $7.79 \pm 1.81\%$ ,  $17.59$   
420  $\pm 7.64\%$ ,  $14.1 \pm 1.07\%$ ,  $7.16 \pm 1.70\%$  and  $5.92 \pm 2.53\%$  of the injected dose per gram  
421 of wet tissues (% ID/g), respectively, and for BCPB-DOX, the values are  $4.41 \pm 0.40\%$ ,

422  $16.73 \pm 1.68\%$ ,  $8.59 \pm 2.03\%$ ,  $3.94 \pm 0.83\%$  and  $6.45 \pm 1.39\%$  ID/g, respectively. In  
423 tumors, the DOX concentrations of BCPB-B-DOX and BCPB-DOX groups reach their  
424 maxima of  $9.38 \pm 1.28\%$  and  $5.75 \pm 1.91\%$  ID/g at 12 h p.i., respectively. Over the 48  
425 h monitoring duration, the tumor area-under-curve (AUC) of BCPB-B-DOX group  
426 reaches  $298.3\%$  ID·h/g, which is 1.78-fold that of BCPB-DOX group ( $167.2\%$  ID·h/g  
427 tumor), confirming the higher tumor targeting ability of BCPB-B-DOX than BCPB-  
428 DOX (Fig. 6h).

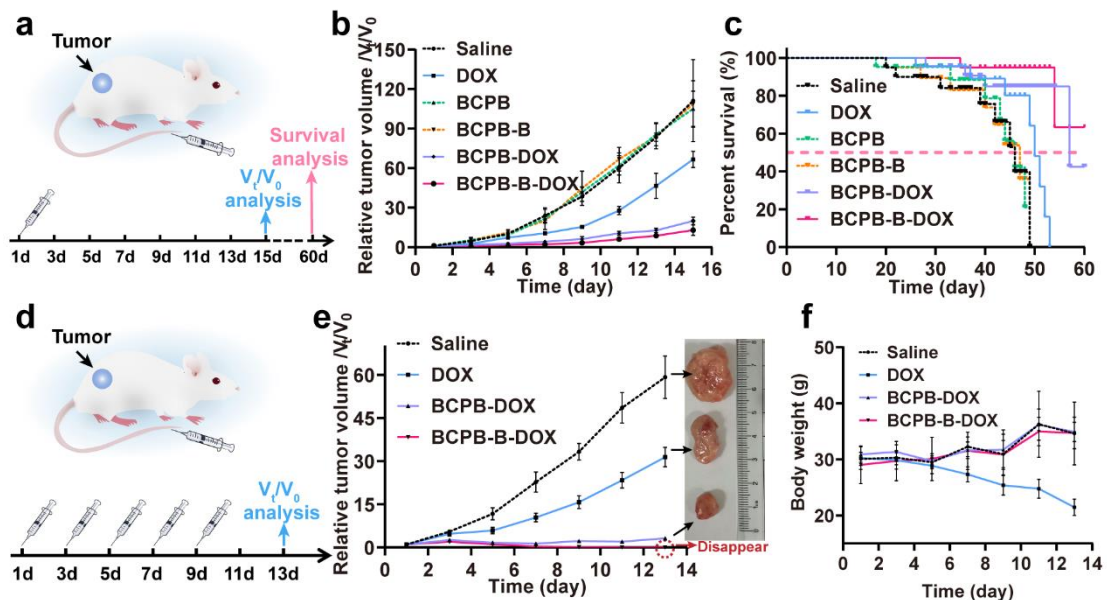
429 **In vivo tumor penetration.** We further checked the in vivo tumor penetration of  
430 BCPB-B and BCPB. After labeled with FITC, the two samples were injected  
431 intravenously into subcutaneous H22 tumor-bearing mice. At 96 h p.i., the tumors were  
432 excised, sectioned with cryostat, and stained immunochemically with anti-CD31. As  
433 observed by CLSM (Fig. 6i), the green signals of BCPB-B almost do not overlap and  
434 keep a distance with the red signals of the vessels, suggesting that most of BCPB-B  
435 have extravasated from the tumor vessels and penetrated further in the tissues. By  
436 contrast, most BCPB still stay around the tumor vessels at the moment, confirming the  
437 higher tumor permeability of BCPB-B than BCPB.

438 **In vivo antitumor effect.** Since BCPB-B exhibits excellent properties in cellular  
439 uptake, lysosome escape, tumor accumulation and penetration, the high antitumor  
440 effectiveness of BCPB-B-DOX is anticipated. Using subcutaneous H22 tumor-bearing  
441 mice as the model animals, we compared the antitumor performance of BCPB-B-DOX,  
442 BCPB-DOX and DOX at a dose of 4 mg/kg DOX equivalent. The mouse groups treated  
443 with BCPB-B, BCPB and normal saline were used as negative control. Each sample

444 was injected as a solution in 0.2 ml of saline via tail vein. The study schedule is  
445 presented in Fig. 7a. The tumor volume and body weight were measured every other  
446 day (Fig. 7b and Supplementary Fig. 29). During the 15-day experiments, the tumors  
447 of the negative control groups grew fastest among all the test groups, and BCPB-B and  
448 BCPB did not show any antitumor activity. For the three DOX formulations, both  
449 BCPB-B-DOX and BCPB-DOX showed much higher tumor suppression effect than  
450 free DOX, and BCPB-B-DOX was better than BCPB-DOX. From the 9<sup>th</sup> day p.i., the  
451 relative tumor volumes of the BCPB-B-DOX and BCPB-DOX groups exhibited a  
452 statistically significant difference ( $P < 0.05$ ). The tumor growth inhibitions (TGIs) on  
453 the 15<sup>th</sup> day p.i. were calculated to be 88%, 82% and 40% for BCPB-B-DOX, BCPB-  
454 DOX and DOX groups, respectively (see Supporting Information for the calculation  
455 method). Based on the body weight evolution with time of all the test groups  
456 (Supplementary Fig. 29), the DOX formulations and the blank brushes did not impose  
457 significant toxicity on the experimental animals, indicating the good biocompatibility  
458 of the polymer brushes and the well-tolerated dose level of DOX. The survival situation  
459 of all the test groups was examined and shown in Fig. 7c. As can be seen, all the mice  
460 in the BCPB-B, BCPB and normal saline groups died within 49 days after the  
461 treatments, and all the mice in the DOX group died within 53 days. By contrast, only  
462 37% and 53% of the mice in the BCPB-B-DOX and BCPB-DOX groups died over the  
463 60-day monitoring duration, respectively.

464 Encouraged by the high antitumor effect of BCPB-B-DOX, we further performed  
465 multiple-dose experiments (dosing every other day at 4 mg/kg DOX equivalent, Fig.

466 7d). After five doses of treatments, all the tumors of BCPB-B-DOX group disappeared  
 467 on the 13<sup>th</sup> day, while the TGIs of BCPB-DOX and DOX groups were 94.6% and 46.9%,  
 468 respectively. Due to the lack of tumor-selective accumulation, free DOX still showed  
 469 poor antitumor effect even after the five-dose treatments. The distinct tumor  
 470 suppression effects of the different formulations are evidenced intuitively by the  
 471 representative photographs of the excised sarcomas (Fig. 7e). Furthermore, as shown  
 472 in Fig. 7f, the body weight evolution with time indicates that BCPB-B-DOX and BCPB-  
 473 DOX did not cause significant toxicity to the mice since their body weights were  
 474 comparable with the saline-treated mice at all the test time points, whereas, the average  
 475 body weight of the DOX group began to decline sharply from the 5<sup>th</sup> day p.i., which  
 476 should result from the even distribution of DOX in bodies that cause significant  
 477 unwanted side effects.



478

479 **Fig. 6 In vivo antitumor effect.** a Illustration of antitumor study schedule with one

480 dose treatment of 4 mg/kg DOX equivalent. b,c Relative tumor volume (b) and survival

481 rate (c) of the H22 tumor-bearing mice after one dose treatment with different protocols  
482 indicated. d Illustration of antitumor study schedule with multiple intravenous  
483 administration with each dose of 4 mg/kg DOX equivalent. e Relative tumor volume of  
484 the H22 tumor-bearing mice treated by five doses with different protocols indicated,  
485 and photographs of the sarcomas excised from the mice on the 13<sup>th</sup> day after the first  
486 treatment. f Body weight change of the H22 tumor-bearing mice treated by five doses  
487 with different protocols indicated. Data are presented as mean  $\pm$  SD (n = 8).

488

## 489 **Discussion**

490 Timely lysosome escape is of paramount importance for the endocytosed  
491 nanomedicines to avoid premature degradation. The existing strategies for lysosome  
492 escape mainly include lysosomal membrane destabilization induced by cationic  
493 materials, lysosome rupture caused by the “proton sponge effect”, membrane fusion  
494 with the cationic liposomes or fusogenic peptides, and membrane damage evoked by  
495 ROS. There are noticeable deficiencies with these strategies. Briefly, the positively  
496 charged materials widely used for lysosome escape are subject to opsonization and  
497 short blood circulation, fusogenic peptides generally suffer function reduction after  
498 conjugation to nanomaterials and are also limited by their high cost and complicated  
499 preparation, and ROS-induced membrane damage is overshadowed by the low tissue  
500 penetration depth of the exciting light. Therefore, developing novel effective lysosome  
501 escape strategy is urgently needed.

502 In this work, we demonstrated clearly that PBA modification could promote greatly  
503 the lysosome escape of CPBs, which further facilitated their exocytosis and transcytosis.  
504 Such phenomena have never been observed before and support the mechanism that the  
505 PBA group improves the tumor permeability of nanomaterials via an active transcytosis  
506 process. Through analyzing the proteins adsorbed by BCPB-B and BCPB after  
507 incubation with tumor cells, we speculate that the specific interactions of the PBA  
508 group with the lysosomal membrane proteins and hot shock proteins may play  
509 important role in the lysosome escape of BCPB-B. Different from the known strategies  
510 for lysosome escape, the strategy of PBA modification does not give rise to significant  
511 adverse effects on the properties of nanomaterials, by contraries, it enhances  
512 remarkably their tumor targeting ability and tumor permeability, which is the featured  
513 advantage of this strategy.

514

515 In conclusion, we synthesized water soluble PBA-modified CPBs and found that  
516 PBA modification could greatly facilitate the lysosome escape of the CPBs, and further  
517 promote their exocytosis and transcellular transfer, imparting higher tumor penetration  
518 than the PBA-free CPBs. We speculate that the mechanism of the PBA-enhanced  
519 lysosome escape is associated with the specific interactions of the PBA group with the  
520 lysosomal membrane proteins and hot shock proteins. DOX was conjugated to the  
521 CPBs via pH-sensitive acylhydrazone linkage with drug loading larger than 20%. By  
522 using the PBA-modified prodrug, the H22 tumor-bearing mice were thoroughly cured  
523 after multiple intravenous administration. This work provided a novel strategy for

524 facilitating the lysosome escape of nanomaterials and a practical design for the CPBs  
525 with high water solubility, high drug loading, and high tumor therapy efficacy.

526

## 527 **Methods**

528 **Synthesis of backbone PGA.** Backbone PGA was synthesized following published  
529 procedures<sup>39</sup>. <sup>1</sup>H NMR (400 MHz, D<sub>2</sub>O) δ (ppm): 0.76-0.93 (d, 3H), 1.76 (m, 2H),  
530 3.29 (s, 2H), 3.88 (m, 3H), 5.50 (s, 1H).

531 **Synthesis of side chain PGMA.** PGMA was synthesized by the ATRP of glycidyl  
532 methacrylate (GMA) with propargyl 2-bromoisobutyrate propargyl 2-bromoisobutyrate  
533 (PBIB)<sup>49</sup> as the initiator. PBIB (88 mg, 0.43 mmol), GMA (10 g, 70.30 mmol), CuBr  
534 (62 mg, 0.43 mmol), PMDETA (74 mg, 0.43 mmol) and anisole (10 mL) were placed  
535 in a 25 mL Schlenk flask followed by freeze-pump-thaw for three cycles in liquid N<sub>2</sub>.  
536 The resulting solution was stirred at room temperature for 2 h. After diluted with DCM,  
537 the resulting solution was filtered through a column of neutral Al<sub>2</sub>O<sub>3</sub> to remove copper  
538 salts. The product was collected and purified by precipitating from DCM to n-hexane 3  
539 times, and dried under vacuum. Yield: 1.50 g (monomer conversion: 16.5%). The  
540 polymerization degree and absolute molecular weight were calculated to be about 27  
541 and 4043 by <sup>1</sup>H NMR, respectively. <sup>1</sup>H NMR (400 MHz, chloroform-*d*) δ (ppm): 0.94-  
542 1.25 (d, 3H), 1.90-2.03 (m, 2H), 2.64 -2.84 (d, 2H), 3.24 (s, 1H), 3.80 (s, 1H), 4.31  
543 (s,1H).

544 **Synthesis of PGMA-PCB-tBu.** PGMA (400 mg, 0.10 mmol), 2-tert-butoxy-N-(2-  
545 (methacryloyloxy)ethyl)-N,N-dimethyl-2-oxoethanaminium (CB-tBu, 4.15 g, 11.80

546 mmol), DMF (10 mL), CuBr (14 mg, 0.10 mmol), and *N,N,N',N',N''*-  
547 pentamethyldiethylenetriamine (PMDETA, 17 mg, 0.10 mmol) were placed in a 25 mL  
548 Schlenk flask followed by freeze-pump-thaw for three cycles in liquid N<sub>2</sub>. The resulting  
549 solution was stirred at room temperature for 24 h. Thereafter, The product was collected  
550 and purified by precipitating from MeOH to the mixture of diethyl ether and acetone  
551 (1:1, v/v) 3 times, and dried under vacuum. Yield: 2.10 g (monomer conversion: 46.7%).  
552 The polymerization degree and absolute molecular weight were calculated to be about  
553 55 and 23418 by <sup>1</sup>H NMR, respectively. <sup>1</sup>H NMR (500 MHz, DMSO-*d*<sub>6</sub>) δ (ppm): 0.81-  
554 1.10 (m, 3H), 1.50 (s, 9H), 1.82-1.90 (d, 2H), 2.66-2.81 (d, 2H), 3.45 (s, 6H), 4.30 (s,  
555 4H), 4.67 (s, 2H, in PCB-tBu).

556 **Synthesis of PGMA-PCB-tBu-POBpin.** PGMA-PCB-tBu (1.50 g, 0.064 mmol),  
557 OEGMA-Bpin<sup>36</sup> (487 mg, 0.84 mmol), DMF (4 mL), MeOH (4 mL), Cu (0) wire (l =  
558 10 cm, d = 1 mm), and PMDETA (11 mg, 0.064 mmol) were placed in a 25 mL Schlenk  
559 flask followed by freeze-pump-thaw for three cycles in liquid N<sub>2</sub>. The resulting mixture  
560 was stirred at 50°C for 24 h. Thereafter, the crude product was purified by precipitating  
561 from MeOH to the mixture of diethyl ether and acetone (1:1, v/v) 3 times, dialyzing  
562 against deionized water and lyophilization successively. Yield: 1.42 g (monomer  
563 conversion: 91.2%). The polymerization degree and absolute molecular weight were  
564 calculated to be about 12 and 30521 by <sup>1</sup>H NMR, respectively. <sup>1</sup>H NMR (500 MHz,  
565 methanol-*d*<sub>4</sub>) δ (ppm): 1.15-1.25 (m, 3H), 1.34 (s, 12H), 1.57 (s, 9H), 2.02 (m, 2H),  
566 3.46 (s, 24H), 3.56 (s, 6H), 4.20 (s, 2H), 4.50 (s, 2H), 7.13-7.70 (m, 4H).

567 **Synthesis of BCPB-EP.** PGMA-PCB-tBu (843 mg, 0.036 mmol), backbone PGA (3.34  
568 mg, 0.018 mmol), CuSO<sub>4</sub>·5H<sub>2</sub>O (0.45 mg, 0.0018 mmol), PMDETA (3 mg, 0.018  
569 mmol), DMF (4 mL), and MeOH (2 mL) was placed in a 10 mL Schlenk flask. After  
570 degassing, a solution of ascorbic acid (6.3 mg, 0.036 mmol) in 1 mL of DMF was added  
571 followed by 3 freeze-pump-thaw cycles. The resulting mixture was stirred at 40°C for  
572 48 h under dark. Thereafter, the crude product was purified by precipitating from  
573 MeOH to acetone 3 times, dialyzing against deionized water and lyophilization  
574 successively. Yield: 683 mg (80.7% conversion rate). <sup>1</sup>H NMR (500 MHz, DMSO-*d*<sub>6</sub>)  
575 δ (ppm): 0.83 (m, 3H), 1.49 (s, 9H), 1.85-1.99 (m, 2H), 2.64-2.81 (d, 2H), 3.53 (s, 6H),  
576 3.92 (s, 2H), 4.31 (s, 2H), 4.67 (s, 2H), 5.57 (s, 1H), 7.23 (s, 1H).

577 **Synthesis of BCPB-B-EP.** PGMA-PCB-tBu-POBpin (1g, 0.036 mmol), backbone  
578 PGA (3.34 mg, 0.018 mmol), CuSO<sub>4</sub>·5H<sub>2</sub>O (0.45 mg, 0.0018 mmol), PMDETA (3 mg,  
579 0.018 mmol), DMF (4 mL), and MeOH (2 mL) were placed in a 10 mL Schlenk flask.  
580 After degassing, a solution of ascorbic acid (6.3 mg, 0.036 mmol) in 1 mL of DMF was  
581 added followed by 3 freeze-pump-thaw cycles. The resulting mixture was stirred at 40°C  
582 for 48 h under dark. Thereafter, the crude product was purified by precipitating from  
583 MeOH to acetone 3 times, dialyzing against deionized water and lyophilization  
584 successively. Yield: 738 mg (73.6% conversion rate). <sup>1</sup>H NMR (400 MHz, methanol-  
585 *d*<sub>4</sub>) δ (ppm): 0.82 (m, 3H), 1.29 (s, 12H), 1.48 (s, 9H), 1.85-2.0 (m, 2H), 2.67-2.81 (d,  
586 2H), 3.34 (m, 30H), 3.73 (s, 2H), 4.32 (s, 2H), 4.71 (s, 2H), 5.32 (s, 1H), 7.89 (s, 1H).

587 **Synthesis of BCPB-N<sub>3</sub> and BCPB-B-N<sub>3</sub>.** BCPB-EP (400 mg, containing 4.66 mmol  
588 epoxy groups), NaN<sub>3</sub> (909 mg, 14 mmol), and ammonium chloride (748 mg, 14 mmol)

589 were dispersed in DMF (25 mL) and stirred at 50°C for 48 h. After removal of the white  
590 precipitate by filtration, the crude product was purified by precipitating from MeOH to  
591 cold diethyl ether 3 times, dialyzing against deionized water and lyophilization  
592 successively to give BCPB-N<sub>3</sub>. Yield: 509 mg (96.8% conversion rate). BCPB-B-N<sub>3</sub>  
593 was obtained by the same procedures as stated above. <sup>1</sup>H NMR (500 MHz, methanol-  
594 *d*<sub>4</sub>) δ (ppm): 0.74-1.18 (m, 3H), 1.60 (s, 9H), 1.98 (m, 2H), 3.29 (s, 6H), 3.95 (m, 4H),  
595 4.40 (s, 2H). BCPB-B-N<sub>3</sub> was obtained following the same procedures as stated above.  
596 <sup>1</sup>H NMR (500 MHz, methanol-*d*<sub>4</sub>) δ (ppm): 1.13 (m, 3H), 1.28 (s, 12H), 1.49 (s, 9H),  
597 2.01 (m, 2H), 3.41-3.45 (m, 30H), 4.00 (s, 2H), 4.13 (m, 2H), 4.43 (s, 2H), 7.71-8.55  
598 (m, 4H).

599 **Synthesis of BCPB-Boc and BCPB-B-Boc.** BCPB-N<sub>3</sub> (509 mg, containing 4.51 mmol  
600 azide groups), PHTe (957 mg, 45.1 mmol, synthesized following published  
601 procedures<sup>36</sup>), CuSO<sub>4</sub>·5H<sub>2</sub>O (11 mg, 0.045 mmol), PMDETA (50 mg, 0.29 mmol),  
602 DMF (4 mL), and MeOH (3mL) were placed in a 10 mL Schlenk flask. After degassing,  
603 a solution of ascorbic acid (158 mg, 0.09 mmol) in 2 mL of DMF was added followed  
604 by 3 freeze-pump-thaw cycles. The resulting mixture was stirred at 40°C for 48 h under  
605 dark. Thereafter, the crude product was purified by precipitating from MeOH to diethyl  
606 ether 3 times, dialyzing against deionized water and lyophilization successively to give  
607 BCPB-Boc. Yield: 590 mg (97.5% conversion rate). <sup>1</sup>H NMR (400 MHz, D<sub>2</sub>O) δ (ppm):  
608 0.76 (m, 3H), 1.17 (s, 9H), 1.50 (s, 9H), 1.99 (m, 2H), 2.40 (s, 2H), 2.60 (s, 2H), 3.37  
609 (s, 6H), 3.97 (s, 4H), 4.41 (s, 2H), 6.91 (s, 1H), 7.22 (s, 1H), 7.78 (s, 1H). BCPB-B-  
610 Boc was obtained following the same procedures as stated above. <sup>1</sup>H NMR (500 MHz,

611 methanol-*d*<sub>4</sub>)  $\delta$  (ppm): 1.13 (m, 3H), 1.29 (s, 12H), 1.49 (s, 3H), 1.65 (s, 9H), 2.04 (m,  
612 2H), 3.40(s, 6H), 4.14 (m, 4H), 4.42 (s, 2H), 8.08 (s, 1H).

613 **Synthesis of BCPB and BCPB-B.** BCPB-Boc (500 mg, containing 3.72 mmol Boc  
614 groups) was dissolved in 10 mL of TFA and stirred at room temperature for 2 h. After  
615 removal of the solvent under reduced pressure, the crude product was purified by  
616 precipitating from methanol to diethyl ether 3 times, and dried under vacuum to give  
617 BCPB. <sup>1</sup>H NMR (400 MHz, D<sub>2</sub>O)  $\delta$  (ppm): 0.77-1.20 (m, 3H), 2.41 (m, 2H), 3.31(s,  
618 6H), 3.97(m, 4H), 4.43 (s, 2H), 7.27 (s, 1H), 7.50 (s, 1H). BCPB-B was obtained  
619 following the same procedures as stated above. (400 MHz, D<sub>2</sub>O)  $\delta$  (ppm): 1.16 (m, 3H),  
620 2.02 (m, 2H), 3.46 (m, 30H), 4.29(m, 6H), 7.35-7.72 (m, 4H).

621 **Synthesis of BCPB-DOX and BCPB-B-DOX.** BCPB (20 mg, 0.15 mmol) and  
622 DOX·HCl (87 mg, 0.034 mmol) were dissolved in 4 mL of trifluoroethanol containing  
623 a drop of TFA. The reaction mixture was stirred at room temperature under dark for 48  
624 h. Thereafter, the crude product was purified by a Sephadex LH-20 column with  
625 trifluoroethanol as an eluant. <sup>1</sup>H NMR (500 MHz, methanol-*d*<sub>4</sub>)  $\delta$  (ppm): 1.11 (m, 3H),  
626 1.29 (s, 3H), 2.02 (m, 2H), 2.85-2.98 (m, 9H), 3.43 (s, 6H), 3.87 (s, 2H), 4.29-4.41 (m,  
627 4H), 5.14-5.45 (m, 3H), 7.62-8.04 (m, 4H). BCPB-B-DOX was obtained following the  
628 same procedures as stated above. <sup>1</sup>H NMR (500 MHz, methanol-*d*<sub>4</sub>)  $\delta$  (ppm): 1.11 (m,  
629 3H), 1.29 (s, 3H), 1.98 (m, 2H), 2.91 (m, 9H), 3.39 (s, 30H), 3.87 (s, 2H), 4.04 (m, 2H),  
630 4.41 (m, 2H), 5.33 (m, 3H), 7.64 (m, 4H). The DOX contents were determined by  
631 measuring the absorbance at 489 nm in water using UV-vis spectroscopy with a pre-

632 established calibration curve. The drug loading contents of BCPB-B-DOX and BCPB-  
633 DOX are about 21% and 23%, respectively.

634 **Statistical analysis.** Statistical results were calculated from at least three independent  
635 experiments and expressed as mean  $\pm$  standard deviation. P values are included to  
636 show the correlation using the Student's t-test. \*p < 0.05 was considered statistically  
637 significant, \*\*p < 0.01, \*\*\*p < 0.001, and \*\*\*\*p < 0.0001 were considered highly  
638 statistically significant.

639

#### 640 **References**

- 641 1. Kashkooli, F. M., Soltani, M. & Souri, M. Controlled anti-cancer drug release  
642 through advanced nano-drug delivery systems: Static and dynamic targeting  
643 strategies. *J. Control. Release* **327**, 316-349 (2020).
- 644 2. Wilhelm, S. *et al.* Analysis of nanoparticle delivery to tumours. *Nat. Rev. Mater.* **1**,  
645 16014 (2016).
- 646 3. Shi, J., Kantoff, P. W., Wooster, R. & Farokhzad, O. C. Cancer nanomedicine:  
647 progress, challenges and opportunities. *Nat. Rev. Cancer* **17**, 20-37 (2017).
- 648 4. Peng, C., Huang, Y. & Zheng, J. Renal clearable nanocarriers: Overcoming the  
649 physiological barriers for precise drug delivery and clearance. *J. Control. Release*  
650 **322**, 64-80 (2020).
- 651 5. Blanco<sup>1</sup>, E., Shen, H. & Ferrari, M. Principles of nanoparticle design for  
652 overcoming biological barriers to drug delivery. *Nat. Biotechnol.* **33**, 941-951

- 653 (2015).
- 654 6. Ahmad, A., Khan, J. M. & Haque, S. Strategies in the design of endosomolytic  
655 agents for facilitating endosomal escape in nanoparticles. *Biochimie* **160**, 61-75  
656 (2019).
- 657 7. Bertrand, N., Wu, J., Xu, X., Kamaly, N. & Farokhzad, O. C. Cancer  
658 nanotechnology: The impact of passive and active targeting in the era of modern  
659 cancer biology. *Adv. Drug Deliv. Rev.* **66**, 2-25 (2014).
- 660 8. Rosenblum, D., Joshi, N., Tao, W., Karp, J. M. & Peer, D. Progress and challenges  
661 towards targeted delivery of cancer therapeutics. *Nat. Commun.* **9**, 1410 (2018).
- 662 9. Pei, D. & Buyanova, M. Overcoming endosomal entrapment in drug delivery.  
663 *Bioconjug. Chem.* **30**, 273-283 (2019).
- 664 10. Selby, L. I., Cortez-Jugo, C. M., Such, G. K. & Johnston, A. P. R. Nanoescapology:  
665 progress toward understanding the endosomal escape of polymeric nanoparticles.  
666 *Wiley Interdiscip. Rev. Nanomed. Nanobiotechnol.* **9**, e1452 (2017).
- 667 11. Varkouhi, A. K., Scholte, M., Storm, G. & Haisma, H. J. Endosomal escape  
668 pathways for delivery of biologicals. *J. Control. Release* **151**, 220-228 (2011).
- 669 12. Andrian, T., Riera, R., Pujals, S. & Albertazzi, L. Nanoscopy for endosomal escape  
670 quantification. *Nanoscale Adv.* **3**, 10-23 (2021).
- 671 13. Wang, S. pH-responsive amphiphilic carboxylate polymers: design and potential  
672 for endosomal escape. *Front. Chem.* **9**, 645297 (2021).
- 673 14. Agirre, M. *et al.* Low Molecular Weight Chitosan (LMWC)-based Polyplexes for  
674 pDNA Delivery: From Bench to Bedside. *Polymers* **6**, 1727-1755 (2014).

- 675 15. Fang, N., Chan, V., Mao, H.-Q. & Leong, K. W. Interactions of phospholipid bilayer  
676 with chitosan: effect of molecular weight and pH. *Biomacromolecules* **2**, 1161-1168  
677 (2001).
- 678 16. Yang, L. *et al.* Poly(2-propylacrylic acid)/poly(lactic-co-glycolic acid) blend  
679 microparticles as a targeted antigen delivery system to direct either CD41<sup>+</sup> or CD81<sup>+</sup>  
680 T cell activation. *Bioeng. Transl. Med.* **2**, 202-211 (2017).
- 681 17. Gu, P. *et al.* Rational Design of PLGA Nanoparticle Vaccine Delivery Systems To  
682 Improve Immune Responses. *Mol. Pharm.* **16**, 5000-5012 (2019).
- 683 18. Hao, F. *et al.* Hybrid micelles containing methotrexate-conjugated polymer and co-  
684 loaded with microRNA-124 for rheumatoid arthritis therapy. *Theranostics* **9**, 5282-  
685 5297 (2019).
- 686 19. Dong, Y. *et al.* Self-assembly of amphiphilic phospholipid peptide dendrimer-based  
687 nanovectors for effective delivery of siRNA therapeutics in prostate cancer therapy.  
688 *J. Control. Release* **322**, 416-425 (2020).
- 689 20. Heitz, M., Javor, S., Darbre, T. & Reymond, J.-L. Stereoselective pH Responsive  
690 Peptide Dendrimers for siRNA Transfection. *Bioconjug. Chem.* **30**, 2165-2182  
691 (2019).
- 692 21. Rayamajhia, S. *et al.* pH-responsive cationic liposome for endosomal escape  
693 mediated drug delivery. *Colloid Surf. B-Biointerfaces* **188**, 110804 (2020).
- 694 22. Li, C., Cao, X. W., Zhao, J. & Wang, F. J. Effective therapeutic drug delivery by  
695 GALA3, an endosomal escape peptide with reduced hydrophobicity. *J. Membr. Biol.*  
696 **253**, 139-152 (2020).

- 697 23. Satoa, Y. *et al.* Understanding structure-activity relationships of pH-sensitive  
698 cationic lipids facilitates the rational identification of promising lipid nanoparticles  
699 for delivering siRNAs in vivo. *J. Control. Release* **295**, 140-152 (2019).
- 700 24. Rangasamia, V. K. *et al.* Exploring membrane permeability of Tomatidine to  
701 enhance lipid mediated nucleic acid transfections. *Biochim. Biophys. Acta-*  
702 *Biomembr.* **1861**, 327-334 (2019).
- 703 25. Qi, T. *et al.* A pH-Activatable nanoparticle for dual-stage precisely mitochondria-  
704 targeted photodynamic anticancer therapy. *Biomaterials* **213**, 119219 (2019).
- 705 26. Yang, G. *et al.* GSH-Activatable NIR Nanoplatform with Mitochondria Targeting  
706 for Enhancing Tumor-Specific Therapy. *ACS Appl. Mater. Interfaces* **11**, 44961-  
707 44969 (2019).
- 708 27. Song, X., Yue, Z., Hong, T., Wang, Z. & Zhang, S. Sandwich-Structured  
709 Upconversion Nanoprobes Coated with a Thin Silica Layer for Mitochondria-  
710 Targeted Cooperative Photodynamic Therapy for Solid Malignant Tumors. *Anal.*  
711 *Chem.* **91**, 8549-8557 (2019).
- 712 28. Zhang, C. *et al.* A Light Responsive Nanoparticle-Based Delivery System Using  
713 Pheophorbide A Graft Polyethylenimine for Dendritic Cell-Based Cancer  
714 Immunotherapy. *Mol. Pharm.* **14**, 1760-1770 (2017).
- 715 29. Soe, T. H., Nanjo, T., Watanabe, K. & Ohtsuki, T. Relation of Photochemical  
716 Internalization to Heat, pH and Ca<sup>2+</sup> Ions. *Photochem. Photobiol.* **95**, 1395-1402  
717 (2019).
- 718 30. Yin, J. *et al.* Tumor targeting and microenvironment-responsive multifunctional

- 719 fusion protein for pro-apoptotic peptide delivery. *Cancer Lett.* **452**, 38-50 (2019).
- 720 31. Sun, Q., Zhu, Y. & Du, J. Recent progress on charge-reversal polymeric  
721 nanocarriers for cancer treatments. *Biomed. Mater.* **16**, 042010 (2021).
- 722 32. Midoux, P. & Monsigny, M. Efficient Gene Transfer by Histidylated  
723 Polylysine/pDNA Complexes. *Bioconjug. Chem.* **10**, 406–411 (1999).
- 724 33. Wu, Q. *et al.* Dual-Functional Supernanoparticles with Microwave Dynamic  
725 Therapy and Microwave Thermal Therapy. *Nano Lett.* **19**, 5277-5286 (2019).
- 726 34. Borodziuk, A. *et al.* Unmodified Rose Bengal photosensitizer conjugated with  
727 NaYF<sub>4</sub>:Yb,Er upconverting nanoparticles for efficient photodynamic therapy.  
728 *Nanotechnology* **31**, 465101 (2020).
- 729 35. Parker, S. The use of diffuse laser photonic energy and indocyanine green  
730 photosensitiser as an adjunct to periodontal therapy. *Br Dent J.* **215**, 167-171 (2013).
- 731 36. Zhang, Y. *et al.* Enhancing tumor penetration and targeting using size-minimized  
732 and zwitterionic nanomedicines. *J. Control. Release* **237**, 115-124 (2016).
- 733 37. Qian, X. *et al.* Targeting and microenvironment-improving of phenylboronic acid-  
734 decorated soy protein nanoparticles with different sizes to tumor. *Theranostics* **9**,  
735 7417-7430 (2019).
- 736 38. Chen, W. *et al.* Phenylboronic acid-incorporated elastin-like polypeptide  
737 nanoparticle drug delivery systems. *Polym. Chem.* **8**, 2105-2114 (2017).
- 738 39. Zhang, Z., Liu, C., Li, C., Wu, W. & Jiang, X. Shape Effects of Cylindrical versus  
739 Spherical Unimolecular Polymer Nanomaterials on in Vitro and in Vivo Behaviors.  
740 *Research* **2019**, 2391486-2391486 (2019).

- 741 40. Zhang, Z. *et al.* Length effects of cylindrical polymer brushes on their in vitro and  
742 in vivo properties. *Biomater. Sci.* **7**, 5124-5131 (2019).
- 743 41. Zhao, W. *et al.* A comprehensive study and comparison of four types of zwitterionic  
744 hydrogels. *J. Mater. Sci.* **53**, 13813-13825 (2018).
- 745 42. Zhu, H., Li, L. & Shen, J. Molecular dynamics simulations suggest conformational  
746 and hydration difference between zwitterionic poly (carboxybetaine methacrylate)  
747 and poly (ethylene glycol). *Chem. Phys.* **532**, 110599 (2020).
- 748 43. Chen, X. *et al.* Differences in Zwitterionic Sulfobetaine and Carboxybetaine  
749 Dextran-Based Hydrogels. *Langmuir* **35**, 1475-1482 (2019).
- 750 44. Keefe, A. J. & Jiang, S. Poly(zwitterionic)protein conjugates offer increased  
751 stability without sacrificing binding affinity or bioactivity. *Nat. Chem.* **4**, 59-63  
752 (2011).
- 753 45. Zhang, X. *et al.* Boronic acid recognition based-gold nanoparticle-labeling strategy  
754 for the assay of sialic acid expression on cancer cell surface by inductively coupled  
755 plasma mass spectrometry. *Analyst* **141**, 1286-1293 (2016).
- 756 46. Tran, M. T. *et al.* A novel role of HSP90 in regulating osteoclastogenesis by  
757 abrogating Rab11b-driven transport. *Biochim. Biophys. Acta-Mol. Cell Res.* **1868**,  
758 119096 (2021).
- 759 47. Gyrd-Hansen, M., Nylandsted, J. & Jäättelä, M. Heat shock protein 70 promotes  
760 cancer cell viability by safeguarding lysosomal integrity. *Cell Cycle* **3**, 1484-1485  
761 (2004).
- 762 48. A, F., Agarraberes & Dice, J. F. A molecular chaperone complex at the lysosomal

763 membrane is required for protein translocation. *J. Cell. Sci.* **114**, 2491-2499 (2001).

764 49. Murtezi, E. & Yagci, Y. Simultaneous photoinduced ATRP and CuAAC reactions  
765 for the synthesis of block copolymers. *Macromol. Rapid Commun.* **35**, 1782–1787  
766 (2014).

767

### 768 **Acknowledgments**

769 This research was supported by the Natural Science Foundation of China (Nos.  
770 51773090, 51422303, and 51973092) and the National Key R&D Program of China  
771 (Nos. 2017YFA0205400, and 2017YFA0701301).

772

### 773 **Author contributions**

774 R.W. and W.W. conceived and designed the research. R.W., C.Y. and C.L. performed  
775 the experiments. Y.S., P.X, J.L. and S.Y. provided helpful suggestions. W.W. and X.J.  
776 analyzed data, edited and revised the paper. W.W. supervised the whole project and  
777 designed the outline.

778

779 **Competing financial interests:** The authors declare no competing financial interests.

780

781

## Supplementary Files

This is a list of supplementary files associated with this preprint. Click to download.

- [WRNNCSI0905.pdf](#)